Weak Gravitational Lensing Analysis on Low-redshift Galaxy Cluster from Hyper Suprime Camera image – Abell 85, Abell 2199 and Abell 119

Hiu Sze, Wu
Department of Physics, the Chinese University of Hong Kong, Shatin, New Territories, Hong Kong

Supervised by: Prof. Dell'Antonio
Department of Physics, Brown University, Providence, RI, U.S.

Abstract

As technological improvements, both software and hardware, help overcome the main sources of error from weak gravitational lensing analysis, the method is implemented to the investigate mass substructure of galaxy clusters and to provide consistency checking for mass distribution. The image from a relatively new camera, Hyper Suprime-Cam (HSC), for Subaru Telescope in Hawaii provided more detail information on background galaxies through deep imaging and was newly released on January. We performed 2-dimensional densitometry to three low-redshift galaxy clusters – Abell 85, Abell 2199 and Abell 119 – using the HSC images and produce the convergence map. LSST pipeline was used for image reduction and measurements. Then, the output catalog was filtered and fitted into fiatmap. The photometric redshift information was not included in this analysis, with justifications. Hence, the result would be useful to locate mass substructure. To determine the mass distribution, more careful and delicate approach is required. Also, this study can be used to check if the HSC image is suitable for weak lensing analysis by consistency check between cameras and methods. This report would introduce basic theory behind the study, then the method used for the study and finally the results and analysis.

1 Introduction

After Albert Einstein published his result on General Relativity, Eddington observed the bending of star light around the Sun during solar eclipse. Later, scientists observed Einstein ring and multiple image of background galaxies around quasar. As these phenomena are not apparent in the universe, scientist extended this method to weak gravitational lensing regime. On the other hand, in the search of cosmological constrains and investigation of dark matter, various methods are used to measure the mass distribution of galaxy cluster in the universe, such as X-ray, assuming hydrostatic equilibrium, or viral velocity, assuming viral equilibrium [1]. Since the assumptions cannot always be justified, weak lensing analysis that free from these assumptions can be used as a measurement tool and consistence check. However, there are several major sources of errors that without the modern technology, weak lensing result would not be accurate enough.

In this study, the images from Hyper Suprime-Cam (HSC) for Subaru Telescope in Hawaii are used for the analysis. The 8.2m large primary mirror of the Subaru telescope is good for deep imaging, as it can receive more light with the same amount of time than other telescopes. This would results in a higher ability to obtain dim galaxies' light, and implies that the galaxies further away from us can be observed. This would greatly beat down the shape noise and lower the chance for intrinsic alignment between background galaxies. At the same time, the combinations of both the telescope and the new camera (HSC) provide a large field of view (FOV) that covers 1.8 $\deg^2$, which would be advantageous for weak lensing analysis to reduce the mass sheet degeneracy. On the software side, the photo reduction pipeline for HSC images are maturer than that for other telescopes. Hence, HSC data were cho-

sen for the analysis. Further discussion of the three mentioned errors would be elaborated in Section 2.

The studied targets and their respective redshift is listed in the table below.

Name	Redshift	Diameter
Abell 85	0.055061 ± 0.000340	69'
Abell 2199	0.030151 ± 0.000230	182'
Abell 119	0.044200	2.0'

Table 1: Galaxy clusters and their respective redshift and diameter. [2]

The chosen galaxy clusters are close to us so that size and magnitude cuts can roughly filter out the foreground galaxies and hence be suffice to estimate their mass distribution.

2 Theory

Gravitational lensing would introduce both magnification, also known as convergence κ, and tangential stretching, known as shear γ, to the background galaxies. Convergence can be given as

$$\kappa(r) = \frac{\Sigma(r)}{\Sigma_{crit}}, \tag{1}$$

where Σ is the surface mass density and Σ_{crit} is the critical surface mass density given by

$$\Sigma_{crit} = \frac{c^2}{4\pi G}\frac{D_L D_S}{D_{LS}}.$$

In strong lensing, the stretching might be very obvious that an arc can be seen, or multiple images are formed. However, in weak lensing, the distortion of background was not as obvious. While the magnification and stretching of a single galaxy is difficult to be determined as the shape of the object is not known, statistically it can be assumed that the background galaxies are randomly oriented and any deviation measured in the average ellipticity of the image would be considered the effect by lensing. This assumption, no intrinsic alignment in the background galaxies, can be justified if the galaxies included in the analysis spread out widely in the cosmos, that is with a wide range of redshifts. In the weak lensing limit, that is $\kappa << 1$, the relationship between average ellipticity and shear is given by

$$\gamma_t \approx \frac{< e_t >}{2}, \tag{2}$$

where γ_t is the tangential shear and $< e_t >$ is the average tangential ellipticity. The error for $< e_t >$, which is called the shape noise, is proportional to $1/\sqrt{n}$, where n is the number of galaxies considerer. There are ways to connect the tangential ellipticity to the mass of the cluster. The relation used in this study is to relate the shear to the convergence, which contain the mass information, by

$$\overline{\kappa}(< r_1) - \overline{\kappa}(r_1 < r < r_2) \approx \frac{2}{1 - r_1^2/r_2^2}\int_{r_1}^{r_2} \gamma d\ln r. \tag{3}$$

This would give the relative convergence between radius smaller than r_1 and between r_1 and r_2. If set the reference $\kappa \to 0$ for $r \to \infty$, then by initially putting $r_2 \to \infty$ we can induce the convergence by repeating the calculation for different radius. In practice, we do not have the information for $r \to \infty$, hence the reference point $\kappa \to 0$ at the boundary of the image. This assumption would be valid if the field of view is large than the diameter of the galaxy cluster. Otherwise, the resulting convergence calculate would be off by a constant, which is named as mass sheet degeneracy. However, this error is not too significant in this study as we concern more at the location of mass substructure, like Abell 2199 which is larger than the field of view as seen in Table 1.

One of the sanity check applied in this project is to calculate the average e_+ and $e_\times$. Let a xy coordinate on the image, then e_+ and $e_\times$ can be defined as in Figure 1. Averaging either e_+ and $e_\times$ should be zero regardless any presence of tangential ellipticity, as the effect should be cancelled out.

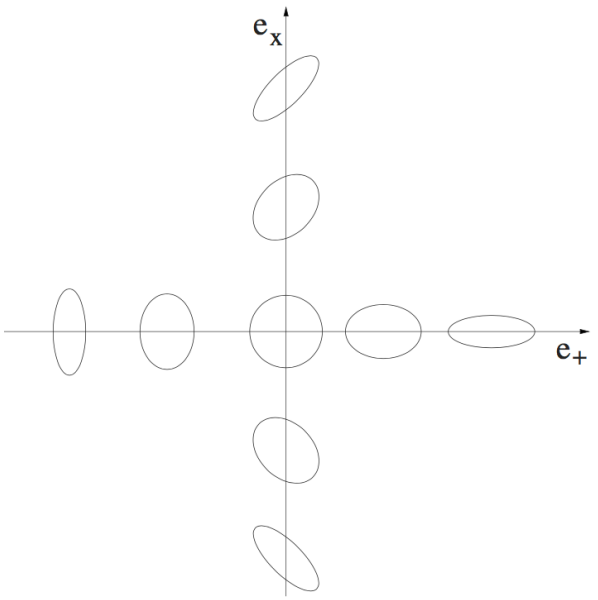

Figure 1: The ellipses representing respective combination of e_+ and $e_\times$. Defining e_+ and $e_\times$ in such a way that given an image, there would be a consistent measurements on using adaptive moments and can be used to calculate the tangential ellipticity by linear combination. Image from [1].

3 Method

For the image processing and catalog output, the Large Synoptics Survey Telescope pipeline was used. The pipeline would first perform reduction on each image for each filter, then mosaic the reduced the image so that the stacking or coaddition of multiple images for one filter would be speeded up. Finally, the coadded image from multiple filters would be analysed and calibrated for consistent astrometry and photometry measurements. The commands and options for each step of the pipeline are listed in Appendix A.

During the processing, the pipeline would return many data products including the calibrated exposures and catalog. The final catalog after the final calibration across filters will be extracted and filtered using Fiat Filters from Fiat Tools developed by Deep Lens Survey. The filter applied are as follow.

An example filter is as follow:

```
(ext_shapeHSM_HsmShapeRegauss_e1)**2+(
    ext_shapeHSM_HsmShapeRegauss_e2)
    **2<1.5 && deblend_nChild==0 &&
    base_CircularApertureFlux_12_0_flag
    ==0 && base_SdssShape_xx+
    base_SdssShape_yy>5.6 &&
    base_SdssShape_xx+base_SdssShape_yy
    <200 &&
    base_PixelFlags_flag_interpolatedCenter
    ==0 && abs(base_PsfFlux_flux-
    base_GaussianFlux_flux)>0.12 &&
    base_GaussianFlux_flux>2.3 &&
    base_PsfFlux_flux>0 &&
    ext_shapeHSM_HsmShapeRegauss_resolution
    >0.5 &&
    base_GaussianFlux_fluxbase_PsfFlux_flux
    >1.1275.
```

And there are many more options available for filtering. For weak lensing, the selection would mainly base on a reasonable ellipticity measurements, that is

```
(ext_shapeHSM_HsmShapeRegauss_e1)**2+(
    ext_shapeHSM_HsmShapeRegauss_e2)
    **2<1.5,
```

the size of the galaxies selected so as to remove large and foreground galaxy or unreasonably small object, that is

```
base_SdssShape_xx+base_SdssShape_yy>5.6
     && base_SdssShape_xx+
    base_SdssShape_yy<200,
```

the flux to remove foreground bright stars or galaxies and dim objects that probably have a bad measurements on shape, that is

```
base_GaussianFlux_flux>2.3.
```

Other filtering that select the galaxies instead of stars includes

```
abs(base_PsfFlux_flux-
    base_GaussianFlux_flux)>0.12,
    ext_shapeHSM_HsmShapeRegauss_resolution
    >0.5,
    base_GaussianFlux_fluxbase_PsfFlux_flux
    >1.1275
```

For each automated filtering, Fiat Review from Fiat Tools was used to check if abnormal or bad selections were performed. Some of the bad measurements cannot be removed, example is shown as in Figure 2. Therefore,

we tried to remove the obvious bad objects, including bright objects or ghosts, manually through Fiat Review. Comparing the catalog before and after remove, the number of object was decreased by roughly 10%, yet the output mass map was very similar. Hence, the significance of bad objects are low and manual removal would be obsolete.

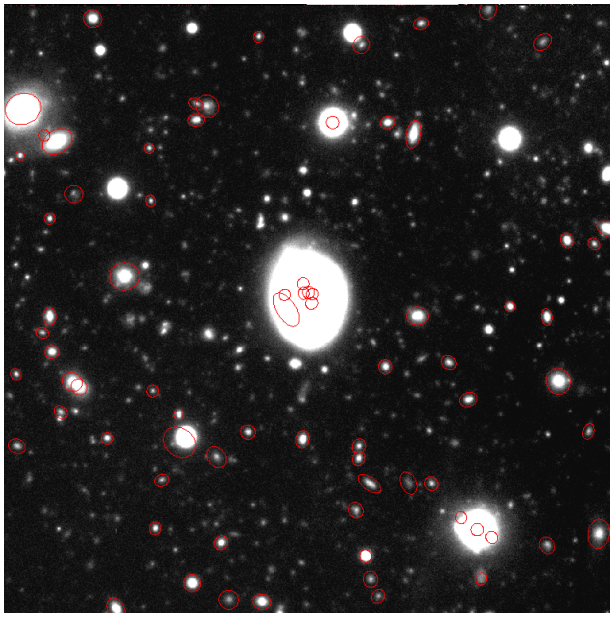

Figure 2: Fiat reviewing on A2199 HSC-G.

Finally, the filtered catalog from each filter was fed into Fiat Map and would be outputting the mass map according to equation (3), which is the radial densitometry. The densitometry was repeated by moving the centre around the image, so as to produce a 2-dimensional mass map. The results would be presented in Result and Analysis section.

4 Result and Analysis

There are five broad-band filters (g-, r-, i-, z-, and Y-band) for the HSC camera as shown in Figure 3 [3]. They replace the r- and i-band filters with r2- and i2-band filters in 2016 [4]. The image data used in this study is prior to the replacement and most of them are g-, i- and r-band.

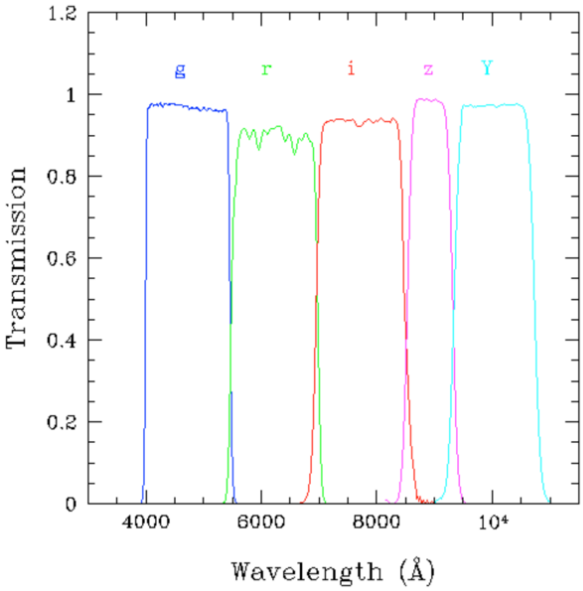

Figure 3: A plot of transmission against wavelength for respective filters.

4.1 Abell 85

Figure 4 shows the calibrated optical image from HSC data. The output image from the LSST pipeline was given as separated patches due to the large size, roughly 6GB in total. Hence, displaying the image using ds9 would require the command line

```
ds9 -mosaic wcs */calexp*.fits
```

which means open the mosaic images and arrange them according to the world coordinate system. The colour scale of separate patches was adjusted according to their own max min values. Hence, a discontinuous brightness across the patches would be observed in the optical images.

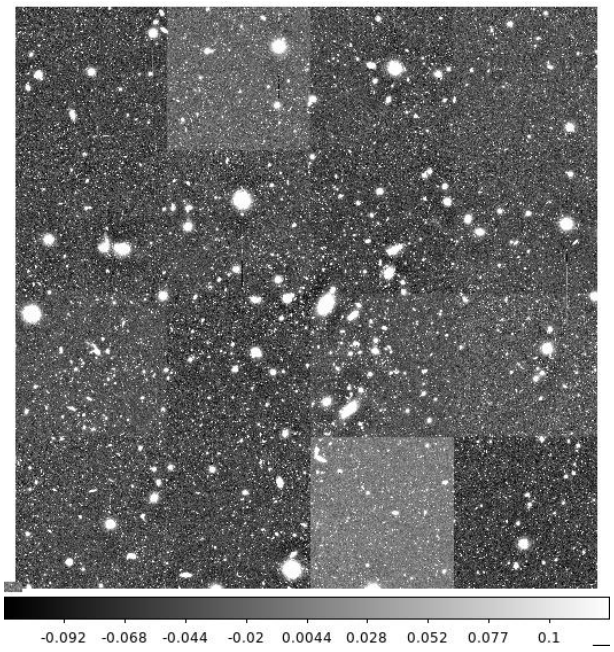

Figure 4: Zoomed optical and coadded image of Abell 85 from HSC data.

From Figure 5, consistency of mass map between difference filters is shown, especially for the peaks around the centre. Note that the peaks around the edge would more likely to be false positive, as the average ellipticity only covers a portions of galaxies around those points.

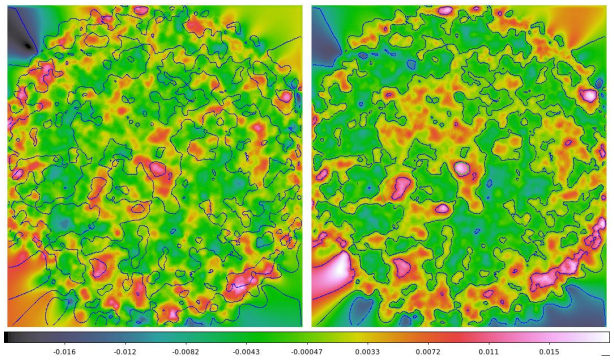

Figure 5: Fiatmap output mass map for Abell 85. Right is the map for I-band with 5 contour levels. Left is the map for G-band with the contour level from the I-band mapped according to the physical coordinate of the image, for the sake of comparison.

The sanity check was listed in Table 2.

	mean e_+	mean $e_\times$
g-band	0.0002190	-0.007874
i-band	-0.002365	-0.008811

Table 2: Mean e_+ and $e_\times$ in different filters for Abell 85

Both catalog for each filter has the average under the tolerance. They were, then used to compare with optical data.

In Figure 6 and 7, the contours were mapped onto the optical image. For R1 region, it can be seen that there are two galaxies overlapping the same region, while in R2 and R3 there are no apparent galaxies the both regions. So the mass substructure might be due to dark matter or dim galaxies in the cluster.

In Figure 8, the results from lensing signal was compared with the X-ray signal. By comparing the purple regions and R2 and R4 regions, no strong coherence is manifested, with the orientation of mass distribution mirrored between the two method. More careful treatments of the lensing signal is needed before any conclusion and assertion. Besides, consistency of lensing signal from different cameras should also be checked.

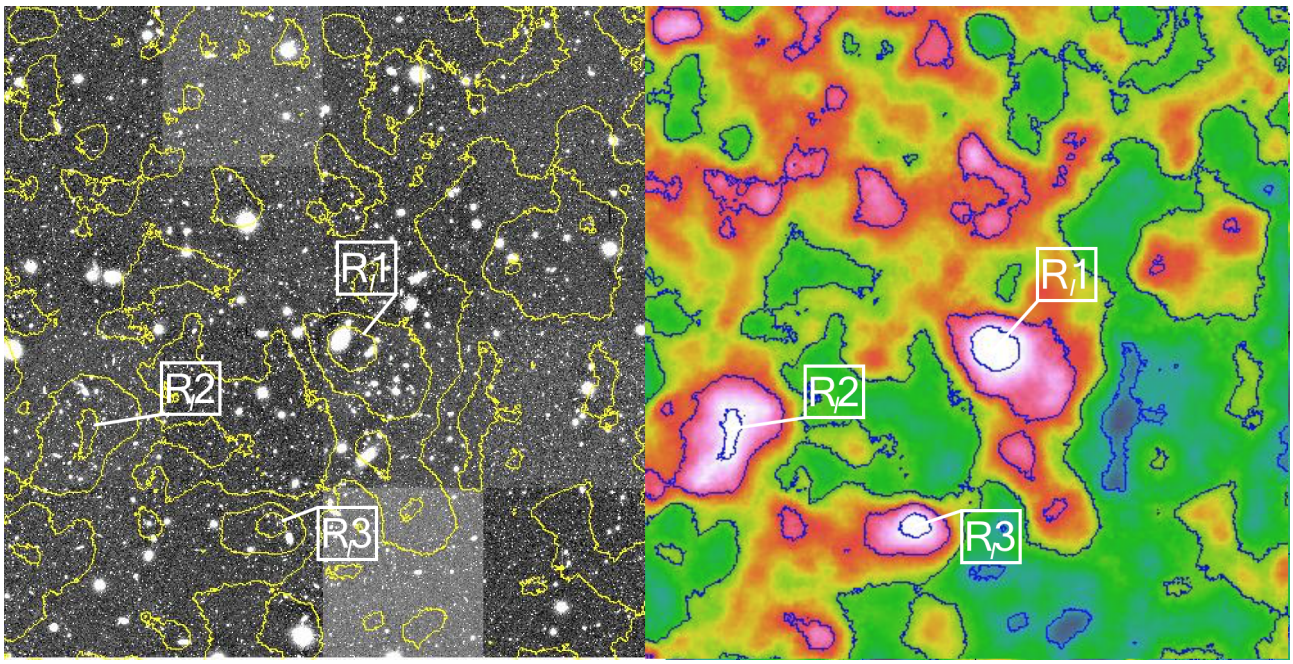

Figure 6: Right is the zoomed map for i-band with 5 contour levels in blue. Left is the optical image from LSST pipeline with the contour level from the i-band mapped onto for comparison. R_I1, R_I2 and R_I3 region are marked on both images.

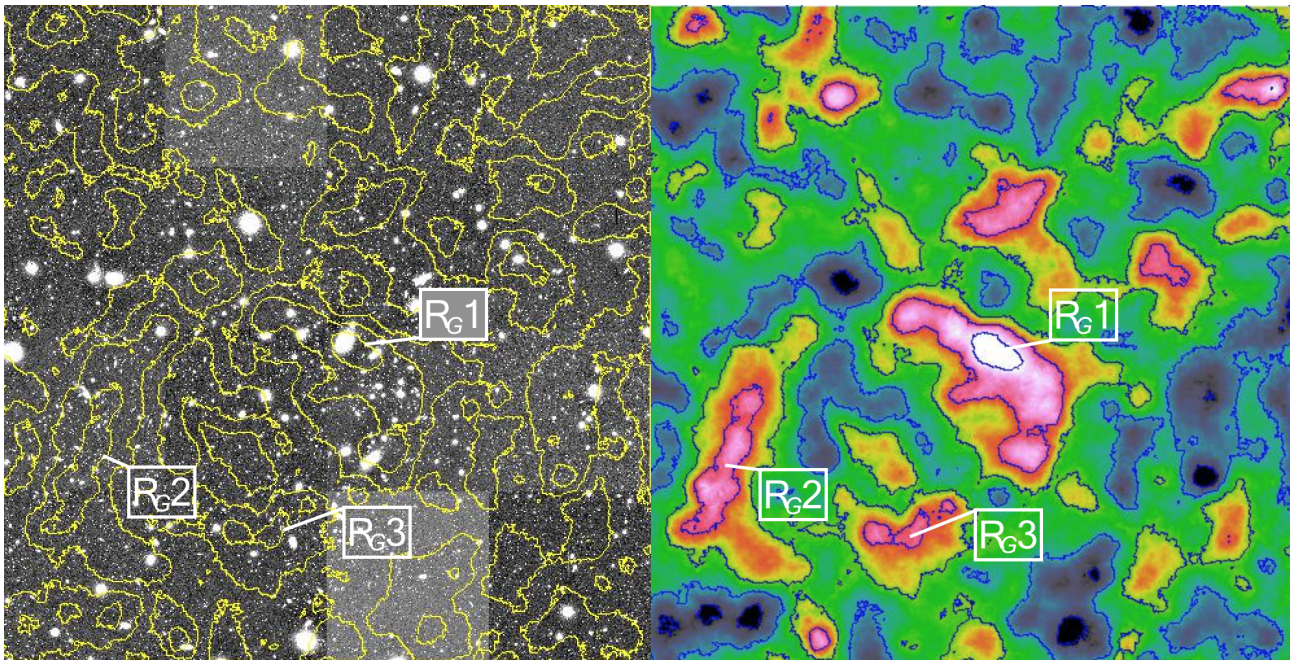

Figure 7: Right is the zoomed map for g-band with 5 contour levels in blue. Left is the optical image from LSST pipeline with the contour level from the g-band mapped onto for comparison. R_G1, R_G2 and R_G3 region are marked on both images.

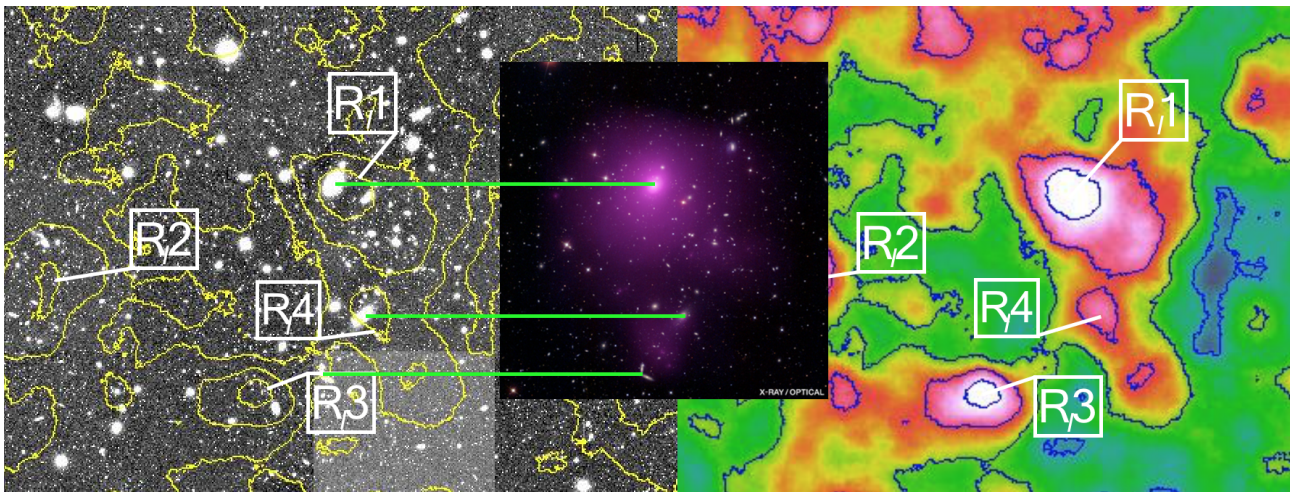

Figure 8: The image in the middle is the image of Abell 85 from Chandra. [3] The purple regions are the X-ray image and it was superimposed onto the optical image. It is now used to compare with the lensing signal in this figure. The green lines are mapping the same objects according to the optical image. The lensing map on the right and the contours are from I-band.

4.2 Abell 2199

This cluster should suffer the most from mass sheet degeneracy as the diameter is about twice the diameter of FOV. However, this cluster is worth analysis as there are mass map from another camera being processed at the same time.

The mosaic optical image is shown in Figure 9.

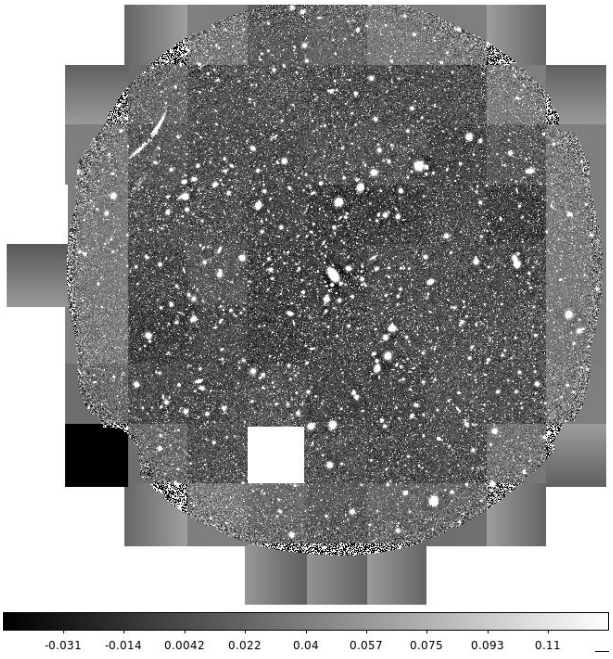

Figure 9: Optical and coadded image of Abell 2199 from HSC data.

The sanity check was listed in the following table.

	mean e_+	mean $e_\times$
g-band	-2.1201×10^{-5}	0.0005236
i-band	0.001747	-0.002572
r-band	0.01204	0.009981

Table 3: Mean e_+ and $e_\times$ in different filters for Abell 2199

In Figure 10, the image shows the map for different filters. Coherence between filters are observed again around the central region. The three small peaks near the center matches with each other. Usually, the filter with lower passband can image the dimmer galaxies as the longer wavelength of light transmit better through obstacles. However, the map from the g-band filter image, which is with shortest wavelength, has the highest resolution. It is due to the number of exposure being stacked together. 19 shots was coadded together for g-band, 10 shots for i-band and 4 shots for r-bands. The number of shots coadded was reflected by the resolution of map produce, which dimmer and dimmer galaxies are able to be measured and accounted for the shearing effect. This might also account for the increasing mean e_+ and $e_\times$, the higher the number of shots coadded, the more galaxies included, the lower

the shape noise and the closer the average ellipticity to be zero.

Figure 11 shows a map of Abell 2199 from another telescope, Canada-France-Hawaii Telescope (CFHT). Due to the difference in scales and resolution, the mapping of contour line is more charllenging. Yet, a consistent pattern, triangular-shape mass distribution, can be observed at the center for both cameras. The map from HSC shows more details than the one from CFHT. The possible reasons are the aperture of telescopes and resolution of pixels. The camera for CFHT is MegaCam and the respective specifications are listed below.

	HSC of Subaru Telescope	MegaCam of CFHT
Aperature of Telescope	8.2 meter	3.6 meter
Pixel Scale	0.185”	0.17”
No. of CCD (2k × 4k)	104	36
FOV deg sq.	≈ 1.77	≈ 0.9
Median seeing	0.6”	0.7”

Table 4: Comparison between HSC of Subaru Telescope and MegaCam of CFHT [5, 6, 7, 8]

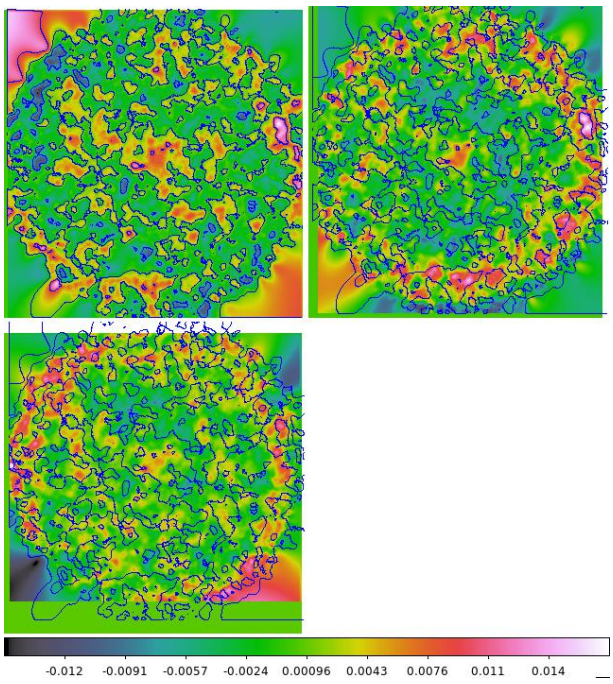

Figure 10: Fiatmap output mass map for Abell 2199. The top left-hand map is the map for g-band with 5 contour levels. The top right-hand map is the map for i-band and the bottom map is the map for r-band. The contour level from g-band is mapped onto the other two map.

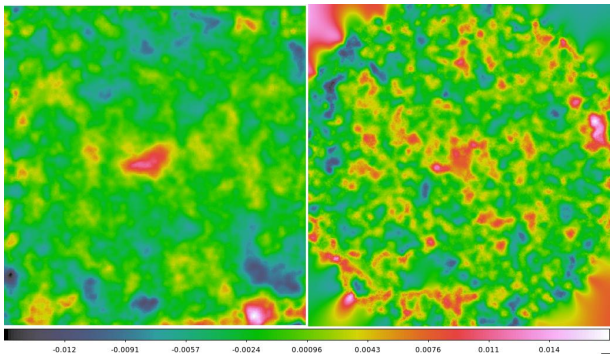

Figure 11: Left is the mass map of Abell 2199 from Canada-France-Hawaii Telescope i-band analysed image data. Right is the map from HSC g-band without contour level.

In Figure 12, the map of HSC g-band, the one with higher resolution among other filters, was selected to compare with the stacked optical image. Again, no apparent galaxies or mass sources overlap with the peaks in the mass map. Since there is consistency between filters and, more importantly, between cameras, so the peaks in the maps

would less likely be false positive. Therefore, this galaxy cluster, Abell 2199, worth a deeper investigation into analysing the mass distribution. However, as mentioned, for careful treatments, image with larger FOV would be needed to avoid mass sheet degeneracy for this galaxy cluster.

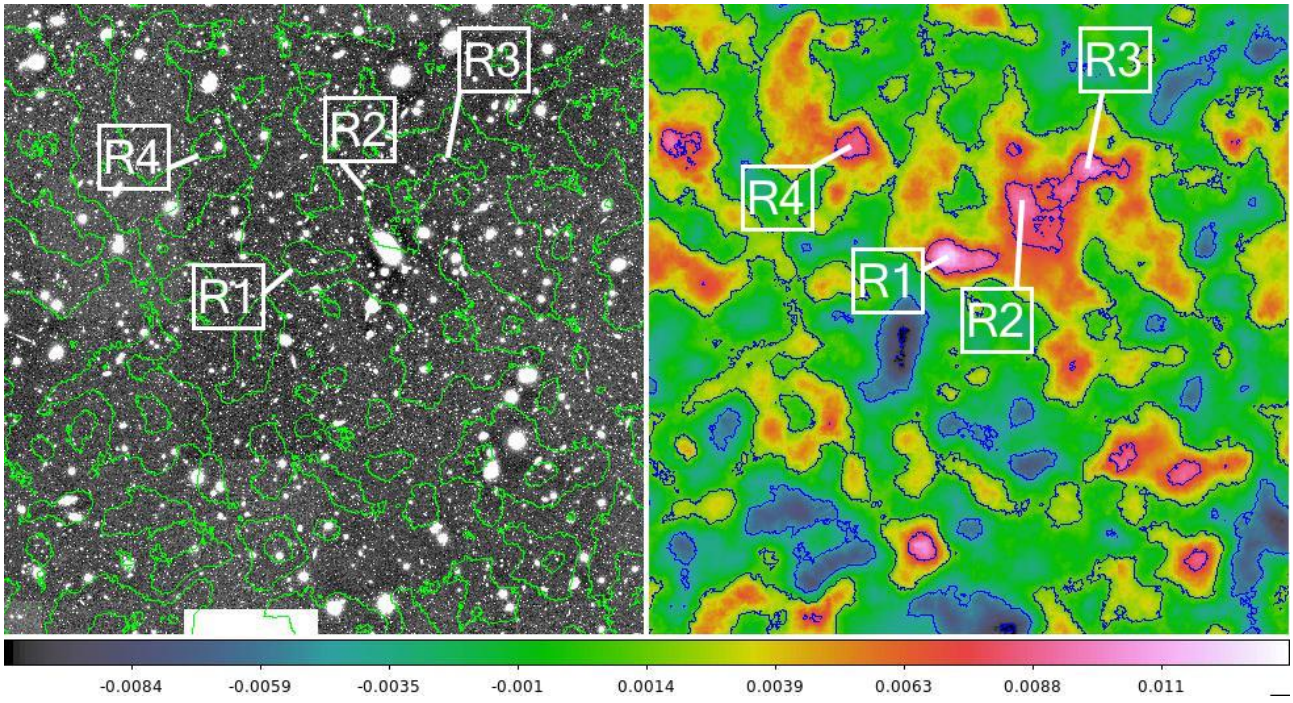

Figure 12: Right is the zoomed map for g-band with 5 contour levels in blue. Left is the optical image from LSST pipeline with the contour level from the g-band mapped onto for comparison. R1, R2, R3 and R4 region are marked on both images.

4.3 Abell 119

The mosaic image and the mass maps are shown below in Figure 13 and 15.

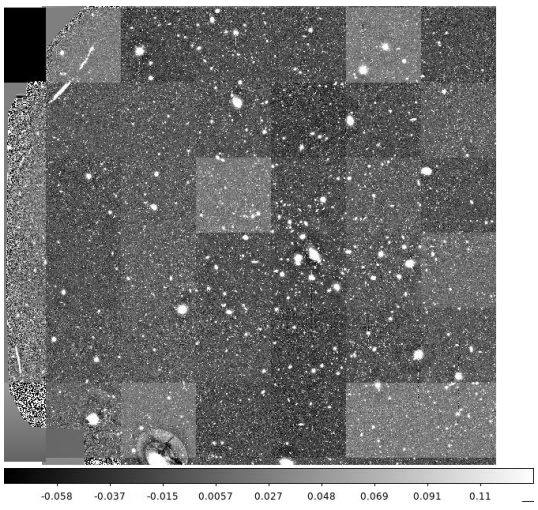

Figure 13: Zoomed optical and coadded image of Abell 119 from HSC data.

Once again, consistency between filters can be seen.

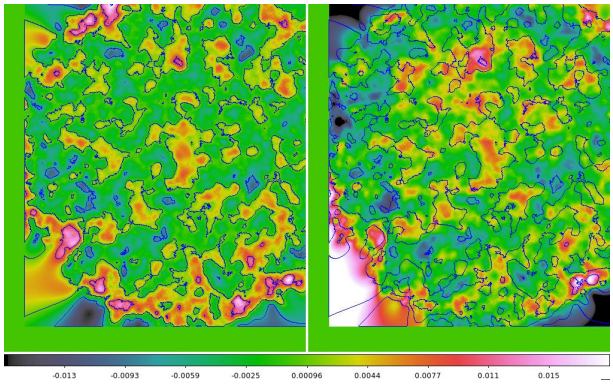

Figure 14: Fiatmap output mass map for Abell 119. Left is the map for g-band with 9 contour levels. Right is the map for i-band with the contour level from g-band mapped onto for comparison.

The sanity check was listed in Table 5.

	mean e_+	mean $e_\times$
g-band	-0.008979	-0.006700
i-band	-0.003523	-0.01288

Table 5: Mean e_+ and $e_\times$ in different filters for Abell 85

The $e_\times$ for i-band is slight higher than the tolerance. For the g-band, 10 exposures were used for the coadd while only 5 for i-band. More sanity checking is needed to confirm which case would be the cause for bad results. Since the i-band catalog exceed the tolerance level, it would not be used to compare with the optical image.

From Figure 15, in R1, there are two bright and probably foreground galaxies in the middle. With redshift information, the mass measurement for individual galaxy can be compared with the mass calculated using weak lensing methods, thus be able to locate and measure dark matters. Hence, more focus can be put in R1. R4 also have some small objects overlapped with the mass map peak. However, without a redshift information, we cannot certified them as foreground galaxies. For other regions, no obvious hypothesis can be drawn.

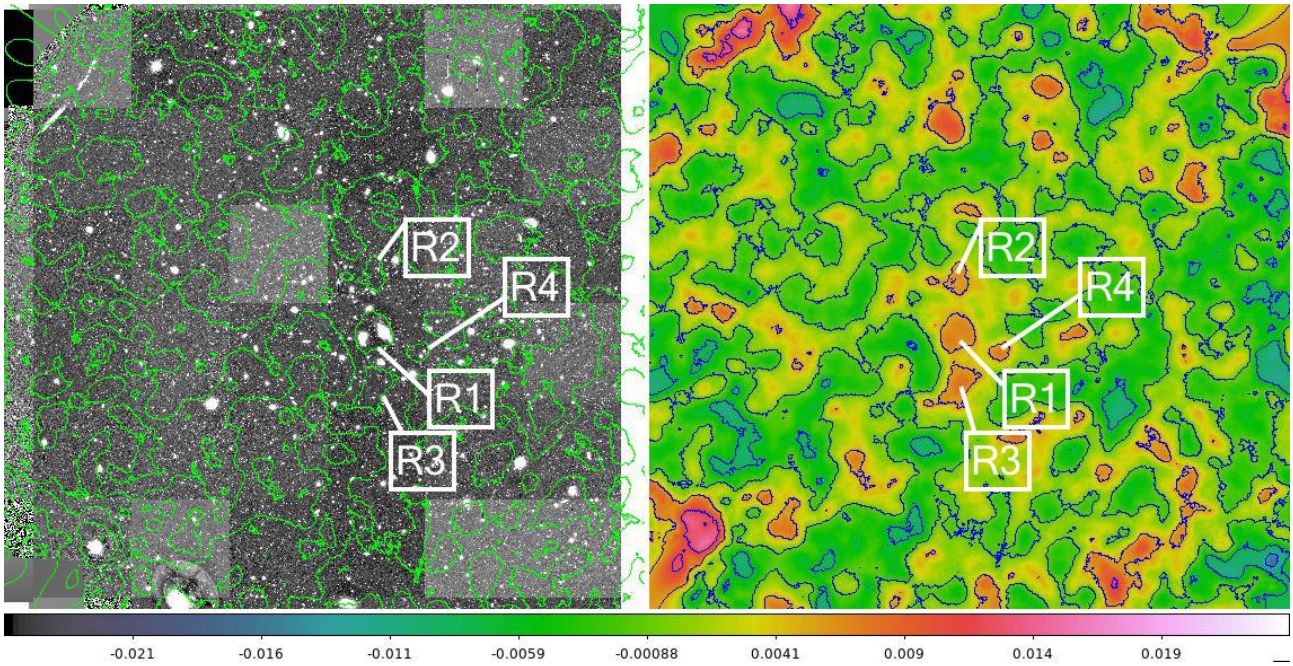

Figure 15: Right is the zoomed map for g-band with 9 contour levels in blue. Left is the optical image from LSST pipeline with the contour level from the g-band mapped onto for comparison. R1, R2, R3 and R4 region are marked on both images.

5 Conclusion

This study roughly shows that the resolution of mass map from the HSC images are relatively higher. The consistency might indicates the images together with the pipeline used could be suitable for weak lensing analysis. However, since redshift information was not included in this study, it could not produce an accurate mass map and draw assertive conclusion on the mass distribution. More careful treatments, such as photometric redshift information, and sanity checking, such as the Gaussian distributions and quantitative B-mode measurements, should be included in the following studies.

6 Acknowledgement

The author would like to thank Prof. Ian Dell'Antonio, Mr Binyang Liu, Mr Shenming Fu, and every fellow-mates in the lab, including Harry S. Chalfin, Elizabeth Chen, Jungho Daniel Choi, RuiXi Seet, Emma C. A. Tilley, and Dr. Jacqueline McCleary from

Brown University for the guidance and advice on the project and the subject. The mentioned method was completed by using the Large Synoptics Survey Telescope pipeline and the fiat tools from Deep Lens Survey. The CFHT data in Figure 11 shown in this report was produced by Emma C. A. Tilley in the group and the sanity checking python programme used was developed by Harry S. Chalfin. The author also like to thank Brown University for the library borrow service.

This programme would not be possible without Prof. MC Chu and the Department of Physics, The Chinese University of Hong Kong. The author is grateful for the financial support from the Brown University, Department of Physics CUHK, CN YANG Scholarship (Research Experience) and Yasumoto SS Ex & UG Research Programme.

References

[1] David Wittman. Weak Lensing. In: Courbin F, Minniti D, editor. Gravitational Lensing: An Astrophysical Tool. 1st ed. Berlin: Springer; 2002. p. 55-92.

[2] NASA/IPAC Extragalactic Database - NED. USA: Jet Propulsion Lab, California Institute of Technology. [accessed 2017 Sep 28]. http://ned.ipac.caltech.edu/.

[3] HSC filter – HSC pipeline manual. Tokyo: National Astronomical Observatory of Japan; 2016 [accessed 2017 Sep 28]. http://hsc.mtk.nao.ac.jp/pipedoc_e/e_hsc/index.html.

[4] HSC filters. Tokyo: National Astronomical Observatory of Japan; c2000-2013 [accessed 2017 Sep 28]. https://www.subarutelescope.org/Observing/Instruments/HSC/sensitivity.html.

[5] MegaPrime/MegaCam - General Specifications & Performance. 2017 [accessed 2017 Sep 28]. http://www.cfht.hawaii.edu/Instruments/Imaging/MegaPrime/generalinformation.html.

[6] About the Canada-France-Hawaii Telescope. Hawaii: CFHT Corporation. [accessed 2017 Sep 28]. http://www.cfht.hawaii.edu/en/about/.

[7] Observing Information – HSC – Subaru. Tokyo: National Astronomical Observatory of Japan; c1999-2011 [accessed 2017 Sep 28]. https://www.naoj.org/Projects/HSC/forobservers.html.

[8] Basic Design – Subaru Telescope Tokyo: National Astronomical Observatory of Japan; c1999 [accessed 2017 Sep 28]. https://subarutelescope.org/Introduction/outline.html.